Promotional role of Mn doping on catalytic oxidation of VOCs over mesoporous TiO$_2$ under vacuum ultraviolet (VUV) irradiation

Yajie Shu [a], Jian Ji [a], Ying Xu [a], Jiguang Deng [b], Haibao Huang [a,*], Miao He [a], Dennis Y.C. Leung [c], Muyan Wu [c], Shengwei Liu [a,*], Shuilian Liu [a], Gaoyuan Liu [a], Ruijie Xie [a], Qiuyu Feng [a], Yujie Zhan [a], Ruimei Fang [a], Xinguo Ye [a]

[a] School of Environmental Science and Engineering, Sun Yat-Sen University, Guangzhou 510275, PR China
[b] College of Environmental and Energy Engineering, Beijing University of Technology, Beijing 100124, PR China
[c] Department of Mechanical Engineering, University of Hong Kong, Hong Kong

ABSTRACT

Volatile organic compounds (VOCs) are the crucial precursors to the formation of fine particulate matter and photochemical smog. Photocatalytic oxidation (PCO) under vacuum ultraviolet (VUV) irradiation has attracted increasing interest for VOCs degradation owing to its strong oxidation capability and excellent stability. However, the generation of O$_3$ from VUV irradiation causes secondary pollution and needs to be addressed. In this study, the Mn doped mesoporous TiO$_2$ (Mn/meso-TiO$_2$) was developed and first combined with VUV irradiation to remove O$_3$ as well as enhance benzene degradation via O$_3$-assited catalytic oxidation. Results indicate that the Mn doped TiO$_2$ exhibited a much higher benzene removal efficiency (82%) than undoped one (70%) and commercial TiO$_2$ P25 (48%). The O$_3$ by-product can be completely eliminated by Mn/meso-TiO$_2$ and contributed to benzene removal efficiency of about 34%. The excellent performance was attributed to the formation of highly reactive oxidizing species such as O(^{1}D), O(^{3}P), hydroxyl radicals (•OH) via catalytic decomposition of O$_3$ over oxygen vacancy sites of Mn oxides. Mn/meso-TiO$_2$ cooperated well with VUV and such a VUV-PCO process is very promising for VOCs degradation.

© 2017 Elsevier B.V. All rights reserved.

1. Introduction

Air pollution, has become a global issue and especially serious in developing countries such as China and India [1,2]. Volatile organic compounds (VOCs) have been proved to be one of the most crucial precursors to the formation of fine particulate matter like PM2.5 and photochemical smog. They are common air pollutants in various indoor environments [3], as well as vehicles emission [4] and industrial processes [5]. Some VOCs, such as toluene, benzene and formaldehyde, are carcinogenic and detrimental to the health and safety of human beings [6,7]. Consequently, great efforts and extensive research have been made to remove VOCs by using adsorption [8], absorption [9], photocatalysis [10–13], biological degradation [14], plasma-catalysis [15], catalytic combustion [16] and some emerging combined processes.

In last two decades, Photocatalytic oxidation (PCO) has been widely studied for degradation of low-concentration VOCs [17]. Recently, PCO with vacuum ultraviolet (VUV) irradiation is considered as a novel and efficient AOP process for VOCs degradation since VUV lamp can generate mercury resonance lines at both 254 nm and 185 nm to improve the light irradiation intensity [18,19]. Compared with the widely-used UV irradiation of 254 nm, VUV lamps using high-purity quartz can allow full transparency for the mercury resonance line at 185 nm. The energetic photons of 185 nm UV can not only activate the photocatalyst but also directly generates numerous reactive species such as O (^{1}D), O(^{3}P), hydroxyl radicals (•OH) and ozone by dissociating oxygen and water vapor [20,21]. It is worth mentioning that these oxidants can efficiently reduce the formation of organic intermediates and their accumulation on the surface of photocatalyst, leading to a high photocatalytic activity and stability.

However, the residual O$_3$ generated by the 185 nm VUV irradiation cause secondary pollution. O$_3$, a major air pollutant, is toxic and harmful to the environment and health of human being. It is well known that O$_3$, as a strong oxidant, can be used for the oxidation

of pollutants under some conditions. Our previous studies [22–25] have demonstrated that O_3 can greatly promote photocatalytic oxidation of benzene. Parrino et al. [26] also revealed that a relatively low rate of photocatalysis (0.3 times the rate of ozonation) is sufficient to get the highest photocatalytic ozonation (PO) synergistic effects between photocatalysis and ozonation. Therefore, it is of great interest to develop multi-functional photocatalysts which can efficiently decompose O_3 and simultaneously enhance VOCs degradation by utilizing residual ozone in the VUV process.

Among various photocatalysts for VOCs abatement, mesoporous TiO_2 has attracted a wide range of attention owing to its abundance, low cost, nontoxicity, chemical stability [27]. In addition, it has been proven to be an efficient UV responsive photocatalysts due to its 3D connected pore network and a large surface area, which is favorable for the diffusion of reactants and products and offering more active sites [28,29]. Unfortunately, the available photocatalysts including mesoporous TiO_2 were generally not efficient in decomposing and utilizing O_3 owing to its large band-gap energy of 3.2 eV and high recombination ratio of photogenerated electron-hole pairs. Recent studies have shown that metal and metal oxides nanoparticles, especially transition metal oxides [30,31], are the promising catalysts for ozone decomposition owing to the presence of a large number of surface-exposed atoms.

In this study, Mn doped mesoporous TiO_2 (Mn/meso-TiO_2) was developed and combined with VUV irradiation to remove the residual O_3 as well as enhance benzene degradation. Its physical and chemical properties were analyzed by XPS, TEM, SEM and UV–vis. The catalytic activities of Mn/meso-TiO_2, was compared with the undoped one with VUV and UV irradiation to clarify the role of Mn doping respectively. It was found that Mn/meso-TiO_2 can completely eliminate the residual O_3 and benzene degradation was greatly enhanced via O_3-assited catalytic oxidation in the VUV-PCO process when compared with the conventional UV-PCO process. The regeneration tests were conducted to evaluate the repeatability and the stability of Mn/meso-TiO_2 in the VUV-PCO.

2. Experimental

2.1. Preparation of photocatalysts

2.1.1. Mesoporous TiO2

Mesoporous TiO_2 was prepared using the one-step hydrolysis method via the following procedures: Tetrabutyltitanate (20 mL) was added into an airtight canister containing 200 mL redistilled water. After aging for 24 h, the slurry was filtered and washed by distilled water. The filter cake was dried at 50 °C for 12 h in a vacuum oven. The dried sample was heated at 400 °C for an hour with a ramping rate of 30 °C/min, and marked as meso-TiO_2.

2.1.2. Manganese (Mn) doped mesoporous TiO2

Mn doped TiO_2 composites were synthesized by impregnation method. The manganese acetate was dissolved into the mixture of 25 mL redistilled water, after stirring for half an hour, 3 g of the prepared meso-TiO_2 was added into the manganese acetate solution under intensive stirring for 12 h, then the slurry was filtered and washed by distilled water. The sample was dried at 80 °C for 12 h in a vacuum oven. The dried sample was heated at 400 °C for an hour with a ramping rate of 30 °C/min, and named as Mn/meso-TiO_2. All catalysts were grounded, tableted, crushed and sieved to 20–40 mesh before use.

2.2. Materials characterization

The surface morphology and crystal structure of the photocatalysts fabricated were characterized with scanning electron microscopy (SEM, Quanta 400, FEI), transmission electron microscopy (TEM) (Tecnai G2 Spirit, FEI), X-ray sprctroscopy (XRD, PANalytical Empyrean X-ray powder diffractometer, 35 kV and 25 mA, Cu Kα). Chemical compositions of the samples were analyzed with X-ray photoelectron spectroscopy (XPS, ThermoFisher Scientific ESCALAB 250Xi, Al Kα). The surface area and pore volumes were obtained from a N_2 adsorption/desorption analysis conducted at 77 K on a Micromeritics Tristar II 3020 system. The UV–vis diffuse reflection spectra (UV-vis DRS) were obtained for the dry-pressed disk samples by using a Scan UV–vis spectrophotometer (UV-2450, Shimadzu) with 100% $BaSO_4$ as a reference. All the samples were degassed at 573 K for 2 h prior to BET measurements.

2.3. Experimental set-up

The schematic diagram of the VUV-PCO system is illustrated in Fig. 1. All experiments were carried out in a fixed-bed continuous-flow reactor with an effective volume of 0.5 L. A quartz tube with inner diameter of 8 mm was placed at the center of the reactor and loaded with the catalysts. Two VUV/UV lamps (4 W, Cnlight) were fixed at both sides of the quartz tube to evaluate the photocatalytic activity of the prepared samples. Benzene and water vapor were generated by bubbling dry air through a thermostatic glass bottle containing liquid benzene and deionized water, respectively. The benzene concentration, humidity and gas flow could be adjusted by the mass flow controllers. A air-flow of 1 L/min containing 25 ppm benzene and a relative humidity of 50% was introduced into the reactor. This relative humidity of 50% was found to be the optimum level in our previous study [32]. 1 g catalyst with 20–40 mesh size was used in the test, corresponding to a gas hourly space velocity (GHSV) of 60 L/g_{cat}·h. The concentrations of benzene, and the CO and CO_2 generated from benzene oxidation were measured by a gas chromatography (GC) (9790II, Fuli) equipped with two flame-ionization detectors (FID). One FID was connected with Rt-Q-BOND PLOT column (30 m × 0.25 mm id, film thickness 10 μm) and used for benzene analysis. The injection and detector temperatures were 100 °C and 250 °C, respectively. The other FID, equipped with a packed column (TDX-01, 3 m × 3 mm) followed by a methanizer, was used to determine the concentrations of CO and CO_2. The gaseous organic intermediates from benzene degradation were identified by GC–MS (GRIFFIN 460, LabTech). The solid-phase intermediates deposited on the catalyst were extracted with a CS_2 solution and then identified by GC–MS. The outlet O_3 concentration was monitored by an ozone analyzer (MC500, IDEAL). The percentage conversion of benzene was calculated by the following equation:

$$\text{Conversion of Benezene } (\%) = \frac{[Benzene]_{inlet} - [Benzene]_{outlet}}{[Benzene]_{inlet}} \times 100$$

where $[Benzene]_{inlet}$ and $[Benzene]_{outlet}$ are the benzene concentrations at inlet and outlet, respectively.

3. Results and discussion

3.1. Characterization of the photocatalysts

3.1.1. Structural and morphological analysis of photocatalysts

Fig. 2 displays the XRD patterns of the as-prepared manganese doped (Mn/meso-TiO_2) and undoped TiO_2 (meso-TiO_2). The commercial TiO_2 (P25, Degussa) was used as the reference catalyst. All the samples show a distinct diffraction peak at $2\theta = 25.2°$, corresponding to the 101 plane of anatase TiO_2 (JCPDS 21-1272). It is observed that both Mn doped or undoped TiO_2 exhibits only peaks from anatase phase TiO_2, while P25 shows peaks both from anatase and rutile phase. Compared with the sharp and narrow diffraction peaks of P25, the diffraction peaks of the Mn doped and undoped TiO_2 are slightly lower and wider, and show quite similar diffraction
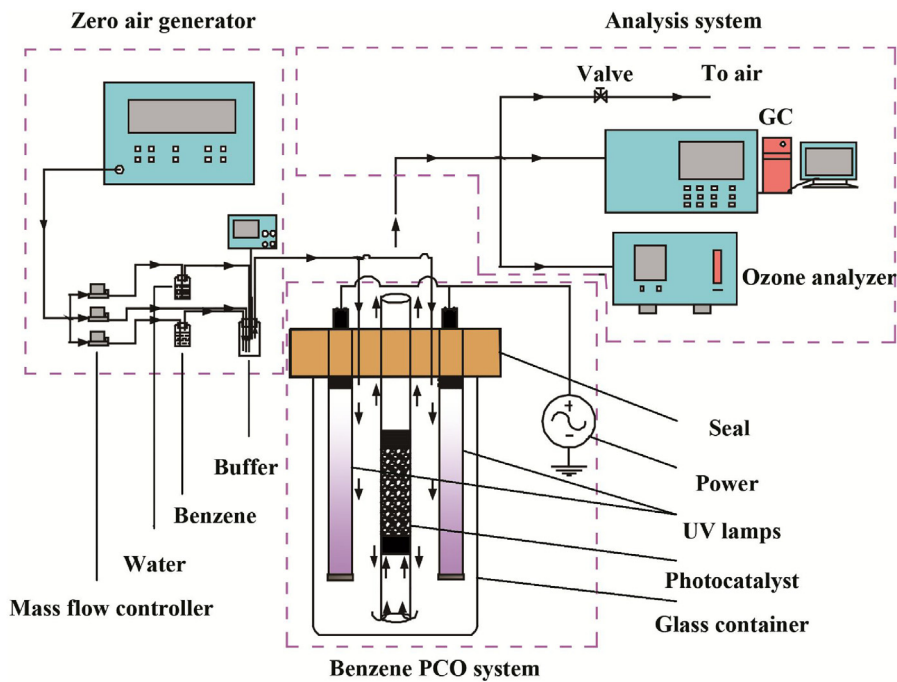
**Fig. 1.** Schematic diagram of VUV-PCO system.
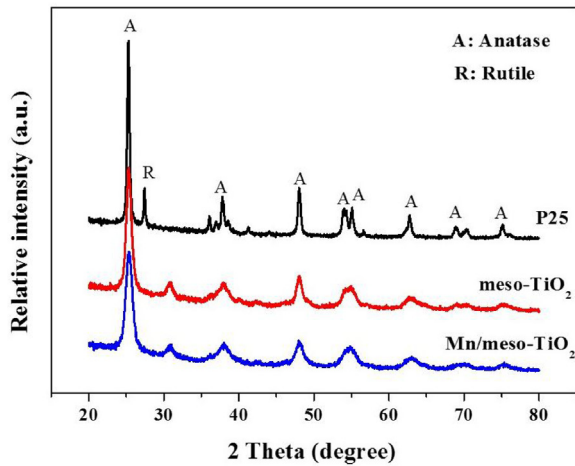
Fig. 2. XRD patterns of different samples.

lines, possibly owing to the mesoporous structure with reduced crystallinity or fine crystallite size. Besides, the phase and structure of the Mn doped mesoporous TiO₂ remained unchanged after incorporating the transition metals. No obvious peaks corresponding to the crystalline Mn_2O_3 or Mn_3O_4 were detected in the XRD patterns of the doped TiO₂. This is possibly ascribed to the low loading amount of the Mn element; or the incorporation of Mn element into the TiO₂ matrix by replacing the Ti ion due to the similar ionic radii of Ti^{4+} and Mn^{4+}/Mn^{3+} [33]. Based on the Scherrer equation [34], the crystallite size of the Mn/meso-TiO₂ is calculated to be about 9.8 nm, while meso-TiO₂ is 11.9 nm, indicating that metal doping may facilitate the dispersion of nanocrystal, refining the particle size.

The structure and morphology of the TiO₂, i.e., P25, meso-TiO₂ and Mn/meso-TiO₂, were examined by TEM and HRTEM, respectively. As can be observed from Fig. 3(a–c), both the meso-TiO₂ and the Mn/meso-TiO₂ exhibit uniform nanocrystalline microstructures with grain sizes of 8–12 nm (Fig. S1), which is consistent

with the results determined from the corresponding XRD patterns. However, P25 shows a rather large grain size from 30 nm to 40 nm. Compared with the meso-TiO₂, the Mn/meso-TiO₂ appears as a little loose agglomeration of nanoparticles. HRTEM analysis (Fig. 3d) was applied to investigate the microstructure of the Mn/meso-TiO. The interplanar lattice spacing is evaluated as 0.35 nm, corresponding to the (101) lattice planes of the anatase TiO₂ (JCPDS card no. 89-4921) [35].

3.1.2. N₂ adsorption-desorption isotherms and pore size distribution

The textural properties, including the Brunauer-Emmett-Teller (BET) specific surface area and the Barrett-Joyner-Halenda (BJH) pore-size distribution curve (inset) of meso-TiO₂ and Mn/meso-TiO₂ are given in Table 1 and Fig. 4, respectively. According to IUPAC classification, the N₂ adsorption-desorption isotherms of both meso-TiO₂ and Mn/meso-TiO₂ display a type IV isotherm with H1-type hysteresis loop at a high relative pressure, suggesting the mesoporous nature of the two samples (2–50 nm in size). Compared with the meso-TiO₂ with very regular mesoporous channels, the Mn/meso-TiO₂ has adsorbed a less quantity with the hysteresis loop shifting approach $P/P_0 = 1$ due to the increased mesopore size[36]. The pore size distribution (the inset in Fig. 4) demonstrates that the meso-TiO₂ has a pore size of 6 nm, while the Mn/meso-TiO₂ possess some slightly larger pores with a sharp peak at about 15 nm. Table 1 lists the pore diameter (dp), pore volume (Vp) and the BET specific surface area of the samples. The meso-TiO₂ microspheres have a higher BET surface area of 125.9 m²/g with a larger pore volume of 0.213 cm³/g. However, after the Mn incorporation, the BET surface area significantly decreased to 67.4 m²/g with a relatively smaller pore volume of 0.197 cm³/g. This result indicated the partial pore blockage by the Mn incorporation. It should be noted that even though some pores maybe blocked, the aggregation and mutual affinity of nano-sized particles are ameliorated with the doping of Mn.
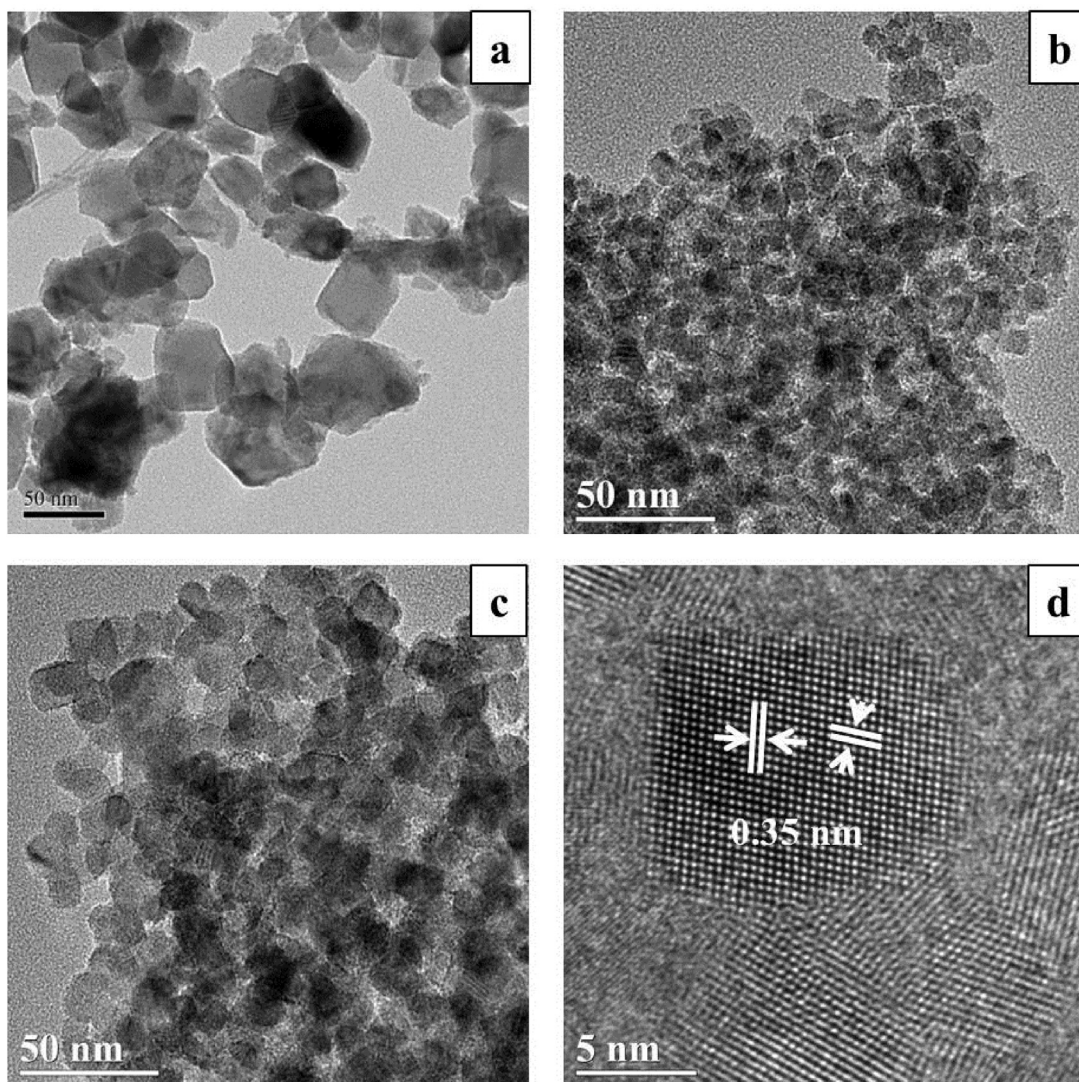
Fig. 3. TEM images of (a) P25; (b) meso-TiO_2; (c) Mn/meso-TiO_2; (d) HRTEM images of Mn/meso-TiO_2 beads.

Table 1
Textural properties of meso-TiO_2 and Mn/meso-TiO_2.

Catalysts	Crystallite size [a] (nm)	Pore diameter [b] (nm)	S_{BET} [c] (m^2/g)	Pore volume [d] (cm^3/g)	Mn content [e] (%)	Mn^{3+}/Mn^{4+} molar ratio [e]
meso-TiO_2	11.9	9.9	125.9	0.213	–	–
Mn/meso-TiO_2	9.8	15.3	67.4	0.197	0.52	0.95

[a] Crystal size calculated by applying the Scherrer equation to the (101) anatase peak.
[b] Average pore diameter, estimated using the desorption branch of the isotherm and the Barrett-Joyner-Halenda (BJH) formula.
[c] BET surface area calculated from the linear part of the BET plot (P/P_0 = 0.05–0.3).
[d] Total pore volume, taken from the volume of N_2 adsorbed at $P/P0$) 0.975.
[e] Mn content and Mn^{3+}/Mn^{4+} molar ratio, taken from the XPS analysis.

3.1.3. XPS analysis

To get an insight into the surface properties, the Mn doped TiO_2 was further investigated by means of X-ray photoelectron spectroscopy (XPS) (Fig. 5) with all the spectra corrected for the C 1s peak at 284.6 eV for determination of binding energy (BE) values. Fig. 5(a) shows the survey scan of the as-synthesized Mn/meso-TiO_2 and the meso-TiO_2 microspheres. Core level XPS signal from C 1s, Ti 2p, and Mn 2p are clearly observed along with Auger signals in the Mn/meso-TiO_2, confirming the presence of Mn in the mesoporous TiO_2 microspheres. As revealed in Fig. 5(b), the X-ray photoelectron spectrum of Ti 2p core electron shows two symmetrical spin-orbit doublet peaks (Ti 2p3/2, binding energy 458.8 eV; Ti

2p1/2, binding energy 464.6 eV) for the undoped and the Mn/meso-TiO_2 microspheres, which are Ti^{4+} in anatase TiO_2. No signature corresponding to other multiple Ti components and any reduced species of titanium such as Ti^{+2} or chemical shift are observed here, suggesting that the Mn doping did not influence the local chemistry of the host Ti atoms in the TiO_2 phase [37].

To identify the ionic state of the Mn and confirm the Mn doping in the TiO_2 lattice, a scan of Mn 2p core level spectra at surface and 3 nm depth by Ar$^+$ ion etching for the Mn/meso-TiO_2 is recorded in Fig. 5(c) and (d), respectively. The broad and asymmetric peaks imply multi-states of Mn in TiO_2. Two states for Mn 2p$_{3/2}$ could be observed, where one major peak located at 641.3 eV indicating the
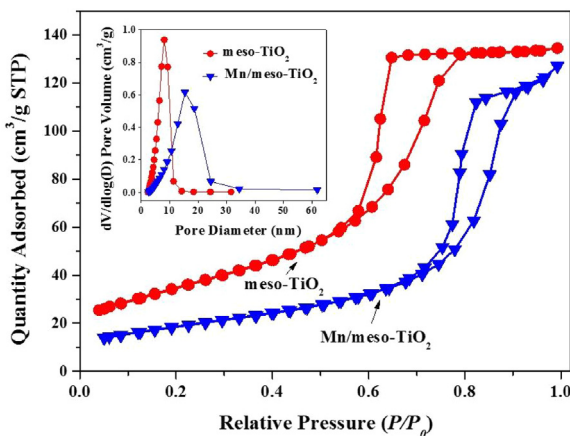
Fig. 4. Nitrogen adsorption–desorption isotherms and the corresponding pore size distribution plots (inset) of the meso-TiO$_2$ and Mn/meso-TiO$_2$.

presence of Mn^{2+} or Mn^{3+}, which agrees well with the reported values, i.e., 641.3e V to 641.9 eV [38,39], and the other one with higher binding energy of 643.1 should be assigned to Mn^{4+}. Since the binding energy of Mn^{2+} and Mn^{3+} are very close to each other (about 641 eV), it is difficult to distinguish Mn^{2+} from Mn^{3+} completely. It

should be noted that, once Mn^{3+} appears in the manganese dioxide, oxygen vacancies will be generated to maintain electrostatic balance according to the process discussed below [40]. Besides, the peak of Mn 2p$_{1/2}$ could also be fitted into two peaks with core levels at 653.1 eV and 654.2 eV, which is attributed to Mn^{3+} and Mn^{4+}, respectively. Regarding the whole Mn 2p peaks, the percentage of Mn^{3+} is about 48.7%, indicating that the oxidation state of the Mn atom may get lower from a high valence environment such as 4+ to slightly above 3+. This is probably attributed to the charge transfer between substitutional and interstitial Mn and the host Ti atoms, as well as the narrowing band gap [41]. Fig. 5(d) presents the Mn 2p XPS at surface and an etching depth of 3 nm, where Mn species can be clearly identified in both bulk and surface, with the content barely varying upon etching. Thus, it is possible that the Mn atoms substitute for Ti atoms at the same site around Ti atoms in the TiO$_2$ bulk. Quantitative analysis implied the Mn/meso-TiO$_2$ bulk had a little higher Mn content (0.71%) versus the surface (0.52%). This suggested that the substitution of Mn for Ti at equilibrium states is favorable, due to similar ionic radii of Mn^{3+}/Mn^{4+} to Ti^{4+} atoms [33].

3.1.4. UV–vis absorption spectra

The UV–vis absorption spectra are illustrated as a function of wavelength for the Mn/meso-TiO$_2$ together with that for the reference pure phase. As is shown in Fig. 6, the absorption spectrum
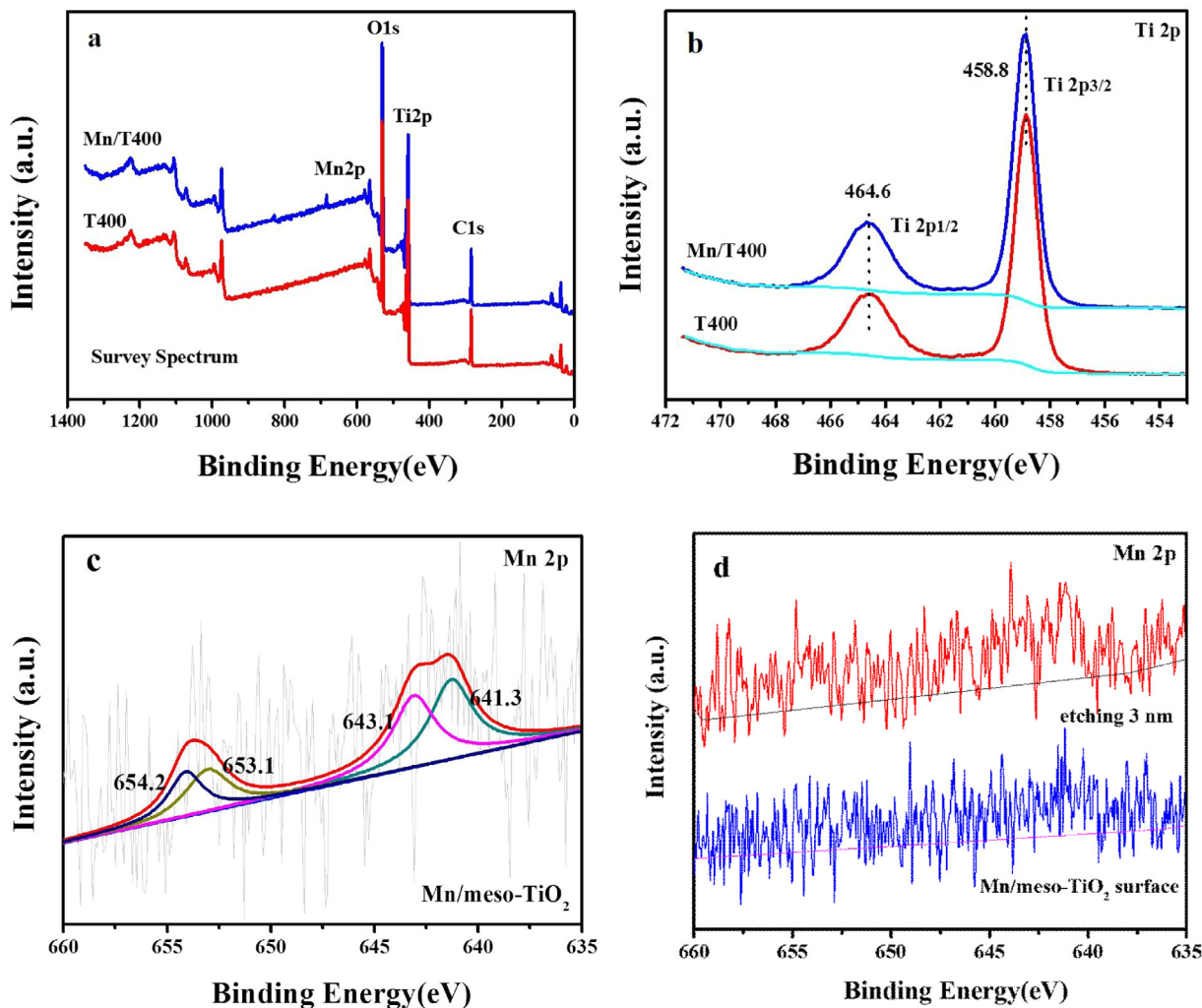

Fig. 5. XPS patterns of (a) survey spectrum; (b) Ti 2p; (c) Mn 2p; (d) Mn 2p of Mn/meso-TiO$_2$ at surface and 3 nm depth by Ar$^+$ ion etching.
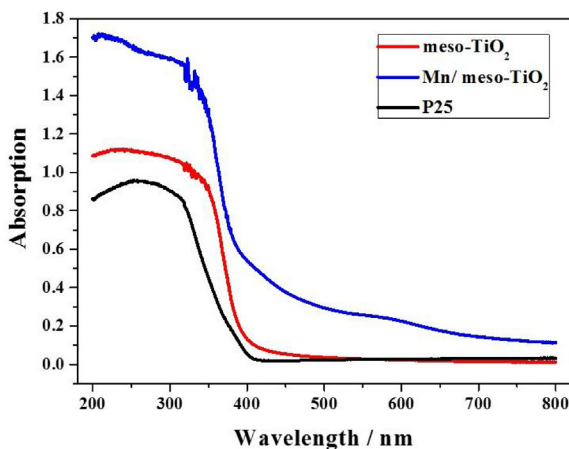
Fig. 6. UV–vis spectrum of different samples.

Fig. 7. Benzene removal efficiency over different samples UV and VUV irradiation.

for P25 and the meso-TiO$_2$ showed a typical absorbance band edge at 200–400 nm region, which corresponded to the intrinsic electron excitation from the valence to the conduction band of the semiconductor. Compared with P25, the mesoporous TiO$_2$ beads (meso-TiO$_2$) had a higher diffuse reflection capability, indicating that pure anatase TiO$_2$ with mesoporous structure has better absorption and utilization capacity of UV irradiation. The results demonstrated that the doping TiO$_2$ with Mn can significantly enhance the light harvesting, ranging from UV light (200 nm) to near infrared light (800 nm) [42], increasing the overlap between light absorption and the solar spectrum, thereby widening the range of sunlight that is able to be captured to generate carriers for photocatalytic reactions. The absorption in the visible region indicated the decrease in band gap and multiple midgap states transitions in the Mn doped TiO$_2$. As the interaction between the t$_{2g}$ state of Mn dopants and Ti atoms, Mn doping could create an additionally occupied state in the bandgap of TiO$_2$ [43]. And the reduction in band gap can be attributed to charge transfer from bulk to surface of the nanocrystals and supports the photogeneration after photo-excitation. The transitions in the visible region can be assigned to Mn^{3+}/Mn^{4+} ions which have migrated into the TiO$_2$ framework due to the d-orbital splitting of Mn in the doped TiO$_2$ [44,45]. With the formation of a Mn^{4+}/Mn^{3+} dopant, energy levels are below the bottom of conduction band of TiO$_2$, and in order to maintain charge neutrality, oxygen vacancies may be generated by doping of Mn^{3+} in the lattice. The results were in agreement with the recent theoretical studies which showed that substitution of Mn ions by Ti^{4+} ions into TiO$_2$ matrix leads to remarkable red shift by both overall reduction of the band gap and introduction of intermediate bands into the forbidden gap [46,47]. According to theoretical calculations, these intermediate levels between the gap are probably due to the energy states that arise in the forbidden zone of energy caused by the presence of transition metal Mn and oxygen vacancies in the TiO$_2$ lattice [48]. Besides, after the introduction of Mn into the TiO$_2$ matrix, the Mn doped mesoporous TiO$_2$ exhibited a pale grey color. Consequently, the increase in the light scattering ability of Mn/meso-TiO$_2$ is important for improving the light-harvesting efficiency.

3.2. Benzene degradation by VUV-PCO system

The performance of the Mn/meso-TiO$_2$ for benzene degradation was evaluated under VUV-PCO and UV-PCO processes. VUV photochemical degradation (without photocatalyst) was also conducted (Fig. 7) for comparison. The outlet concentrations of O$_3$ and CO$_X$ in the VUV-PCO process were presented in Figs. 8 and 9, respectively.
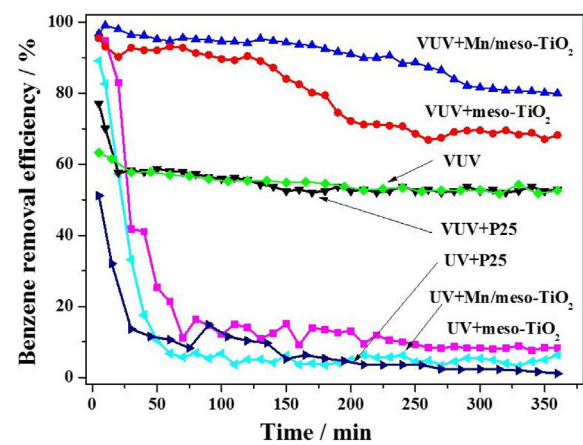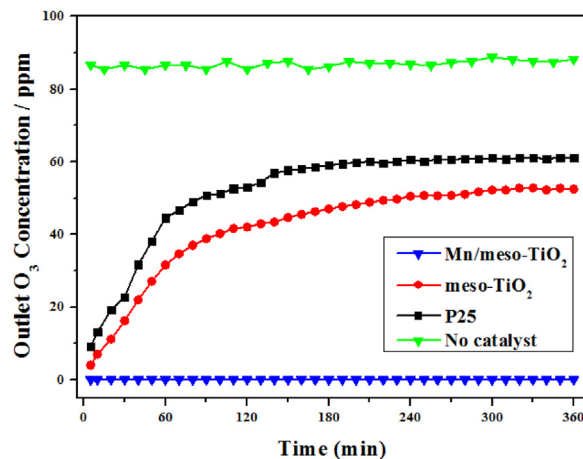

Fig. 8. Outlet O$_3$ concentration of different samples in the VUV-PCO system.
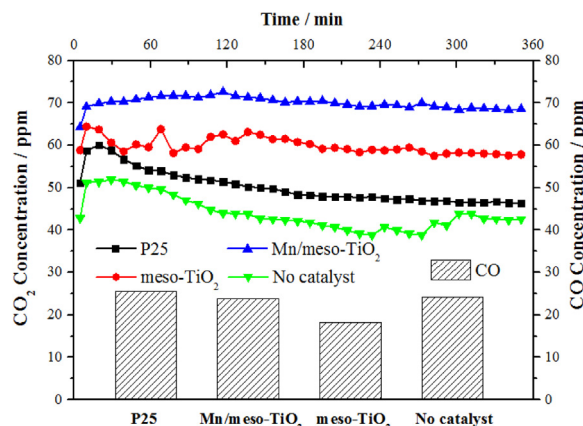

Fig. 9. CO$_X$ concentration of different samples in the VUV-PCO system.

As can be seen in Fig. 7, benzene removal efficiency was increased with the order of UV+ P25 < UV+Mn/meso-TiO$_2$ < UV+ meso-TiO$_2$ < VUV photolysis < VUV+P25 < VUV+ meso-TiO$_2$ < VUV+ Mn/meso-TiO$_2$. Compared with P25, meso-TiO$_2$ exhibited better photocatalytic activity towards benzene oxidation under UV irradiation. Benzene removal efficiency quickly dropped to less than 5% over P25 while it kept stably at about 10% over meso-TiO$_2$. In addition, it is interesting to find that VUV-PCO process achieved a much higher benzene removal efficiency than conventional UV-PCO process. It sharply dropped to 5–10% in the first 60 min over various

samples in the UV-PCO process while kept higher than 50% in all the VUV-PCO process. Among them, P25 showed the poorest catalytic activity towards benzene degradation under VUV irradiation. Its benzene removal efficiency is quickly decreased and nearly close to that without any catalysts, indicating that P25 is not effective under VUV irradiation. However, it reached 96% at the initial stage over meso-TiO$_2$ partially due to the adsorption effect of the catalysts. It was gradually decreased and kept at about 70% after reaction for about 200 min. The stable benzene removal efficiency was further increased to about 82% over Mn/meso-TiO$_2$, indicating that the mesoporous structure cooperated well with VUV irradiation for benzene degradation.

Unfortunately, much O$_3$ byproduct was generated under VUV irradiation, which reached 85 ppm by VUV photolysis alone (Fig. 8). Energetic photons emitted by the VUV irradiation with the maximum emission at 185 nm which are absorbed by oxygen in the air and produced ozone as follows [49,50]:

$$O_2 + h\nu(185 \text{ nm}) \rightarrow O(^3P) + O(^1D) \qquad (1)$$

$$O_2 + O(^3P) \rightarrow O_3 \qquad (2)$$
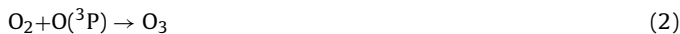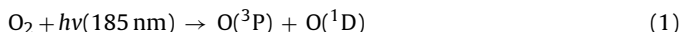
As a good electron acceptor, O$_3$ can effectively prevent the recombination of electron-hole pairs and prolong the lifetime of the holes in photocatalysis [51]. Therefore, it is interesting to take good use of the O$_3$ byproduct for VOC degradation. However, there are still much residual O$_3$ after the addition of P25 and the meso-TiO$_2$ (Fig. 8). Recent studies have shown that metal oxides nanoparticles, especially manganese oxides, are efficient for catalytic decomposition of O$_3$ to generate active oxygen species to enhance VOCs oxidation[52,53]. It is reported that, the catalytic decomposition mechanism of ozone is closely related to the involvement and recycling of oxygen vacancy[30]. The ozone molecule was bounded to Mn/meso-TiO$_2$ surface by inserting an O atom into an oxygen vacancy site. The oxygen vacancy transferred 2-electron to an O atom of ozone, thus forming an oxygen species (O$^-$) and an oxygen molecule (Eq. (3)). At the same time, another ozone molecule reacted with O$^-$ to produce a gas-phase oxygen molecule and a bridging O$_2$ dimer (peroxide, O$_2^-$) (Eq. (4)). Finally, the peroxide species (O$_2^-$) was decomposed to release an oxygen molecule, and consequently the oxygen vacancy is recovered (Eq. (5)), which can participate in the VOCs oxidation or next cycle of O$_3$ decomposition, O$_2^-$ can also react with H$_2$O, generating •OH for VOCs oxidation (Eq. (6)) [17,19,52].

$$O_3 + V_O \rightarrow O^- + O_2 \qquad (3)$$

$$O_3 + O^- \rightarrow O_2^- + O_2 \qquad (4)$$

$$O_2^- \rightarrow V_O + O_2 \qquad (5)$$

$$O_2^- + H_2O \rightarrow 2\text{•OH} \qquad (6)$$
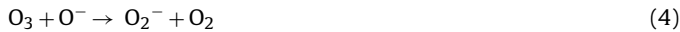
V$_O$ refers to oxygen vacancy site

Fig. 8 shows the outlet ozone concentration over different samples. About 85 ppm O$_3$ was generated under the VUV irradiation. It dropped to 60 ppm over commercially-available P25 and 50 ppm over meso-TiO$_2$, respectively, indicating that they are efficient for catalytic decomposition of O$_3$. It is interesting to find that the O$_3$ concentration was kept at almost 0 ppm throughout the whole reaction over meso-TiO$_2$. Therefore, the Mn doping of meso-TiO$_2$ can greatly facilitate O$_3$ decomposition.

Our previous researches[24,54] have also proposed that VOC abatement in the VUV-PCO process was not only ascribed to the photocatalytic oxidation and photolysis, but also to catalytic ozonation. It was supposed that gaseous benzene was initially degraded via photolysis in the gase-phase since highly active species, such as hydroxyl radical and O$_3$, were generated by the irradiation of energetic photons of 185 nm. VUV photolysis contributed ∼48% benzene

removal efficiency. The residual benzene was further oxidized by photocatalytic oxidation and ozone-assisted catalytic oxidation (OZCO) in the gas-solid phase. It is believed that the key step of the VOCs catalytic abatement is the formation of active intermediate oxygen species (O$^-$/O$_2^-$) which could be generated on the catalyst by ozone decomposition. Besides, the pores and the high surface area of the mesoporous structure (meso-TiO$_2$), as shown in Table 1, can serve as reservoirs for the intermediate active species and the residual ozone by holding them in the adsorbed phase[55]. Consequently, the photocatalysis and ozonation synergistically contributes to the high catalytic activity toward benzene degradation in the VUV-PCO process.

In order to study the benzene catalytic oxidation capacity of in the VUV-PCO process, the outlet CO$_x$ concentration generated from benzene degradation was measured. As shown in Fig. 9, the Mn/meso-TiO$_2$, with the best ozone decomposition capacity, achieved the highest photocatalytic efficiency for benzene degradation (82%) and CO$_x$ concentration. The stable outlet CO$_x$ concentration over the different samples followed the order: P25 < meso-TiO$_2$ < Mn/meso-TiO$_2$, which is same as the order of benzene removal efficiency over them. Unfortunately, if all the removed benzene (∼20 ppm) was completely mineralized into CO or CO$_2$, about 120 ppm COx should be generated. However, only nearly 90 ppm CO$_x$ was formed over the Mn/meso-TiO$_2$, indicating that some trace intermediates were generated from the benzene degradation. It should be noted that the outlet CO concentration of all samples were stable and close to 25 ppm, suggesting that CO is normally generated from VUV photolysis.

3.3. In-situ regeneration of Mn/meso-TiO$_2$

The incomplete oxidation of VOCs generated some organic intermediates, and the accumulation of intermediates on the surface of catalysts would lead to the catalytic deactivation. As shown in Fig. 7 and Fig. S2, benzene removal efficiency over Mn/meso-TiO$_2$ was decreased from about 100% to 82% after VUV irradiation for 300 min, indicating the slow catalytic deactivation. Therefore, it is very important to regenerate the photocatalysts. After reaction for 360 min, benzene flow was cut off and only pure air continued to flow through the reactor to oxidize the intermediates by sustaining VUV irradiation. Although there was no benzene introduced, the outlet CO$_2$ concentration reached nearly 50 ppm and slowly dropped with time. This indicated that the organic intermediates on the catalysts were gradually oxidized. Nearly no CO was formed during the regeneration processes, confirming that CO generally came from the VUV photolysis of gaseous benzene. O$_3$ was reported to adsorb UV light and decompose to form reactive species and hydroxyl radicals which can breakdown carbon deposits and oxidize intermediate on the surface of catalyst [56]. As can be seen in Fig. 10, the outlet ozone concentration stably keeps zero before regeneration for 400 min and gradually increased, demonstrating that O$_3$ is deeply involved in the oxidation of carbon deposits. With the decreased intermediates, O$_3$ appeared and gradually increased after regeneration for 400 min. As the organic intermediates was removed from the surface of catalysts, the active site like oxygen vacancy of the Mn/meso-TiO$_2$ can be recovered. It can be found that benzene removal efficiency over Mn/meso-TiO$_2$ was again increased to nearly 95% over the regenerated Mn/meso-TiO$_2$ as benzene was introduced into the reactor (Fig. S2) and the outlet concentration of CO$_2$ and CO again reached 70 ppm and 20 ppm, respectively. This demonstrated that the deactivated Mn/meso-TiO$_2$ can be easily regenerated in the VUV-PCO system via sustaining VUV irradiation. Slight drop of catalytic activity was also observed during the 3 cycles of benzene catalytic oxidation
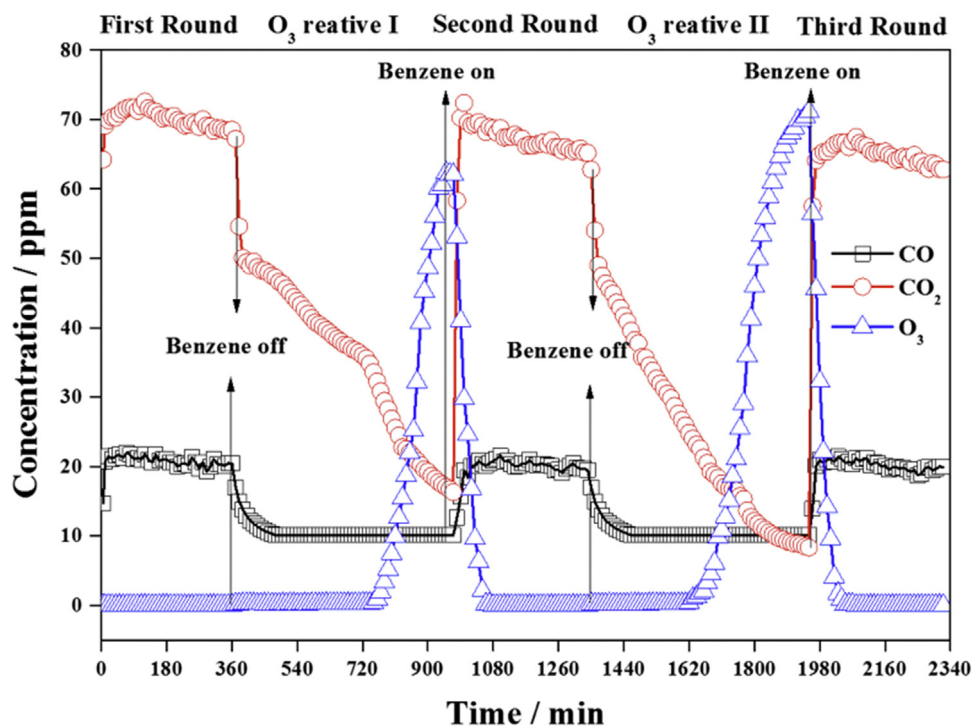
Fig. 10. Outlet CO_x and O_3 concentration of Mn/meso-TiO$_2$ during repeated test in the VUV-PCO system.
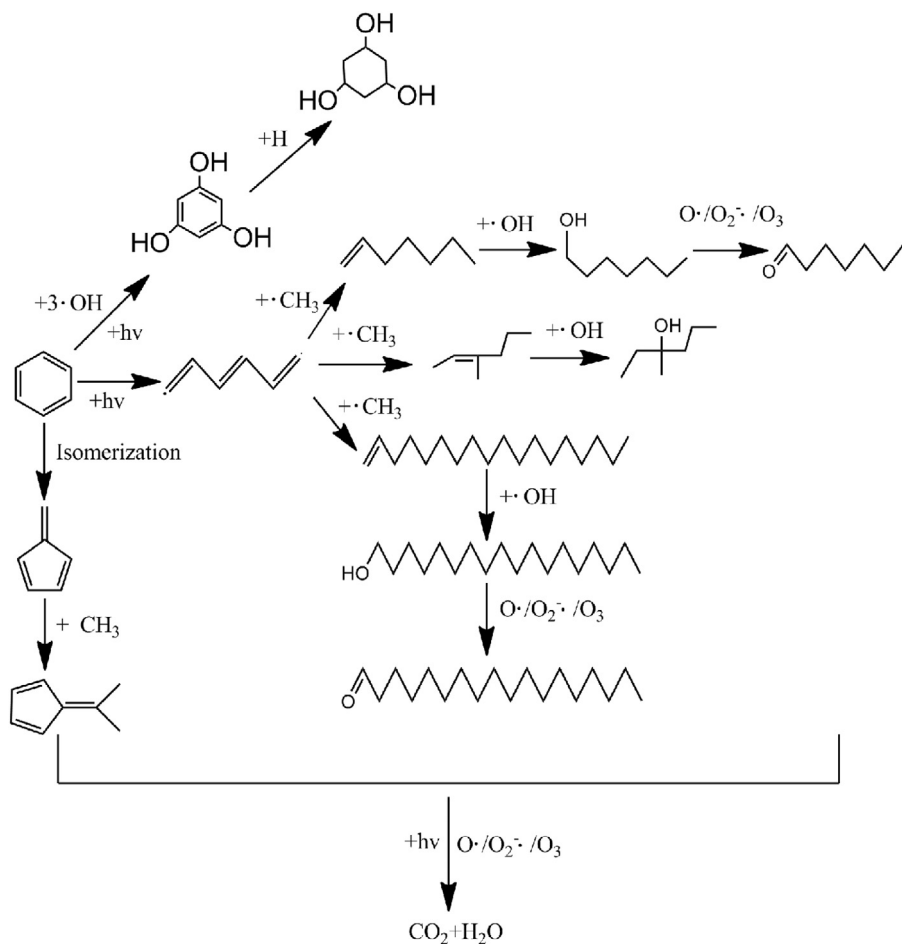
Fig. 11. Degradation process of benzene under VUV-PCO process.

and catalytic regeneration, indicating that the catalyst would partly deactivated and oxygen vacancies were not completely recovered.

3.4. Mechanism and pathway of benzene degradation under VUV-PCO process

Different mechanism and pathway of benzene degradation were proposed according to the identified intermediates in previous study [24,25]. However, the mechanism of benzene degradation was still unclear in VUV-PCO process. In VUV-PCO process, the reactive species such as $O(^1D)$, $O(^3P)$, hydroxyl radicals ($\bullet OH$) and ozone which were generated from VUV irradiation can directly degrade the gaseous benzene at first, then residual benzene, as well as intermediates and ozone, flowed through the catalyst bed to go further catalytic oxidation. Thus, the oxidation of benzene not only happened in the bulk of the gas-phase (e.g. VUV/O_3) but also occurred on the surface of photocatalyst (e.g. VUV/TiO_2 and O_3/TiO_2). In order to make clear the mechanism and degradation pathways, the gaseous intermediates (gas-phase) and adsorbed intermediates on catalysts (solid-phase) were investigated by GC–MS, respectively. Compared with many by-products from benzene in VUV photolysis, no obvious peaks of gas-phase by-products can be detected in the GC–MS chromatograms under VUV-PCO process. This suggested that the intermediates generated by VUV photolysis could be further adsorbed and degraded on the surface of catalyst, eventually oxidized into non-toxic H_2O and CO_2 in VUV-PCO process. Taken together, the possible pathway of benzene degradation in the VUV-PCO was proposed according to the identified products and by-products, as is shown in Fig. 11. On the one hand, through a series of process such as splitting of benzene, hydrogenation, and H abstraction by OH radicals, benzene was degraded into six-member ring cyclitols and aldehydes ketones etc. [57], on the other hand, a class of fulvene was formed by isomerization [58] under the VUV illumination. Above all, the intermediates are easy to be further degraded and mineralized into CO_2 and H_2O.

4. Conclusions

Multi-function Mn/meso-TiO$_2$ was successfully developed and combined with VUV irradiation to remove the O$_3$ byproduct as well as enhance benzene degradation via O$_3$-assited catalytic oxidation. Results indicate that the Mn doped meso-TiO$_2$ exhibited a higher benzene removal efficiency (82%) than the undoped one (70%) and commercial P25 (48%). The O$_3$ by-product can be completely eliminated and contributed to benzene removal efficiency of about 34% with the help of by Mn/meso-TiO$_2$. The excellent performance was ascribed to the formation of highly reactive oxidizing species such as $O(^1D)$, $O(^3P)$, hydroxyl radicals ($\bullet OH$) via catalytic decomposition of O$_3$ over oxygen vacancy sites of Mn oxides. The deactivated Mn/meso-TiO$_2$ can be easily regenerated in the VUV-PCO system via sustaining VUV irradiation. Mn/meso-TiO$_2$ cooperated well with VUV and such a VUV-PCO process is very promising for VOCs degradation.

Acknowledgements

Appendix A. Supplementary data

Supplementary data associated with this article can be found, in the online version, at http://dx.doi.org/10.1016/j.apcatb.2017.08.019.

References

[1] M. Liu, Y. Huang, Z. Ma, Z. Jin, X. Liu, H. Wang, Y. Liu, J. Wang, M. Jantunen, J. Bi, Environ. Int. 98 (2016) 75–81.
[2] L. Cong, C. Yang, Y. Zhao, Z. Ma, J. Bi, L. Yang, M. Xia, Y. Wang, C. Jing, H. Kan, Environ. Int. 416 (2016) 92–93.
[3] U. Schlink, A. Thiem, T. Kohajda, M. Richter, K. Strebel, Sci. Total Environ. 408 (2010) 38–40.
[4] Y. Pang, M. Fuentes, P. Rieger, Atmos. Environ. 83 (2014) 127–135.
[5] J. Zheng, Y. Yu, Z. Mo, Z. Zhang, X. Wang, S. Yin, K. Peng, Y. Yang, X. Feng, H. Cai, Sci. Total Environ. 127 (2013) 456–457.
[6] M.F. Mustafa, Y. Liu, Z. Duan, H. Guo, S. Xu, H. Wang, W. Lu, J. Hazard. Mater. 327 (2017) 35–43.
[7] A. Amann, B.L. Costello, W. Miekisch, J. Schubert, B. Buszewski, J. Pleil, N. Ratcliffe, T. Risby, J. Breath. Res. 8 (2014) 034001.
[8] F. Qu, L. Zhu, K. Yang, J. Hazard. Mater. 170 (2009) 7–12.
[9] B. Ozturk, D. Yilmaz, Process. Saf. Environ. 84 (2006) 391–398.
[10] G. Moussavi, M. Mahdavianpour, J. Chem. Eng. 295 (2016) 57–63.
[11] H. Huang, P. Hu, H. Huang, J. Chen, X. Ye, D.Y.C. Leung, J. Chem. Eng. 252 (2014) 320–326.
[12] B.K. Sang, S.C. Hong, Appl. Catal. B: Environ. 35 (2002) 305–315.
[13] S. Weon, J. Choi, T. Park, W. Choi, Appl. Catal. B: Environ. 205 (2017) 386–392.
[14] W.H. Chen, W.B. Yang, C.S. Yuan, J.C. Yang, Q.L. Zhao, Chemosphere 103 (2014) 92.
[15] X. Xu, P. Wang, W. Xu, J. Wu, L. Chen, M. Fu, D. Ye, J. Chem. Eng. 283 (2016) 276–284.
[16] S. Scirè, S. Minicò, C. Crisafulli, C. Satriano, A. Pistone, Appl. Catal. B: Environ. 40 (2003) 43–49.
[17] P. Fu, P. Zhang, L. Jia, Appl. Catal. B: Environ. 105 (2011) 220–228.
[18] M. Li, Z. Qiang, P. Hou, J.R. Bolton, J. Qu, P. Li, C. Wang, Environ. Sci. Technol. 50 (2016).
[19] T. Ochiai, K. Masuko, S. Tago, R. Nakano, Y. Niitsu, G. Kobayashi, K. Horio, K. Nakata, T. Murakami, M. Hara, Chem. Eng. J. 218 (2013) 327–332.
[20] K. Zoschke, H. Börnick, E. Worch, Water Res. 52 (2014) 131–145.
[21] M. Li, Z. Qiang, C. Pulgarin, Appl. Catal. B: Environ. 187 (2016) 83–89.
[22] H. Huang, W. Huang, Y. Xu, X. Ye, M. Wu, Q. Shao, G. Ou, Z. Peng, J. Shi, J. Chen, Catal. Today 258 (2015) 627–633.
[23] H. Huang, H. Huang, Z. Lu, H. Peng, X. Ye, D.Y.C. Leung, J. Chem. Eng. 259 (2015) 534–541.
[24] H. Huang, H. Huang, Y. Zhan, G. Liu, X. Wang, H. Lu, X. Liang, Q. Feng, D.Y.C. Leung, Appl. Catal. B: Environ. 186 (2016) 62–68.
[25] H. Huang, H. Huang, Q. Feng, G. Liu, Y. Zhan, M. Wu, H. Lu, Y. Shu, D.Y.C. Leung, Appl. Catal. B: Environ. 203 (2017) 870–878.
[26] F. Parrino, G. Camera-Roda, V. Loddo, V. Augugliaro, L. Palmisano, Appl. Catal. B: Environ. 178 (2015) 37–43.
[27] C.A. Korologos, M.D. Nikolaki, C.N. Zerva, C.J. Philippopoulos, S.G. Poulopoulos, J. Photochem. Photobiol. A 244 (2012) 24–31.
[28] D. Chen, F. Huang, Y.B. Cheng, R.A. Caruso, Adv. Mater. 21 (2009) 2206–2210.
[29] W. Zhou, H. Fu, ChemCatChem 5 (2013) 885–894.
[30] Y. Liu, P. Zhang, Appl. Catal. A 530 (2017) 102–110.
[31] J. Nawrocki, L. Fijołek, Appl. Catal. B: Environ. 142–143 (2013) 533–537.
[32] H. Huang, H. Huang, L. Zhang, P. Hu, X. Ye, D.Y. Leung, J. Chem. Eng. 259 (2015) 534–541.
[33] L. Feng, H. Jiang, M. Zou, F. Xiong, A.S. Ganeshraja, E. Pervaiz, Y. Liu, S. Zou, M. Yang, J. Nanopart. Res. 18 (2016) 278.
[34] Q. Zhang, L. Gao, J. Guo, Appl. Catal. B: Environ. 26 (2000) 207–215.
[35] Y. Yan, S. Sun, Y. Song, X. Yan, W. Guan, X. Liu, W. Shi, ACS Nano 7 (2013) 2532–2540.
[36] K.S.W. Sing, Pure Appl. Chem. 54 (1982) 2201–2218.
[37] L. Zhang, L. Zhu, L. Hu, Y. Li, H. Song, Z. Ye, RSC Adv. 6 (2016).
[38] Q.R. Deng, X.H. Xia, M.L. Guo, Y. Gao, G. Shao, Mater. Lett. 65 (2011) 2051–2054.
[39] B. Murugan, A.V. Ramaswamy, J. Phys. Chem. C 112 (2008) 20429–20442.
[40] F. Wang, H. Dai, J. Deng, G. Bai, K. Ji, Y. Liu, Environ. Sci. Technol. 46 (2012) 4034–4041.
[41] S. Sharma, S. Chaudhary, S.C. Kashyap, S.K. Sharma, J. Appl. Phys. 109 (2011) 951.
[42] L. Lu, X. Xia, J.K. Luo, G. Shao, J. Phys. D Appl. Phys. 45 (2012) 485102–485109 (485108).
[43] B. Liu, M. Chen, C. Liu, S.C. Andrews, C. Hahn, D. Yang, J. Am. Chem. Soc. 135 (2013) 9995–9998.
[44] N. Roy, Y. Sohn, K.T. Leung, D. Pradhan, J. Phys. Chem. C 118 (2014) 29499–29506.
[45] A.K. Tripathi, M.C. Mathpal, P. Kumar, M.K. Singh, M.A.G. Soler, A. Agarwal, J. Alloys Comp. 622 (2015) 37–47.
[46] M. Harb, J. Phys. Chem. C 117 (2013) 12942–12948.

[47] B. Leedahl, D.A. Zatsepin, D.W. Boukhvalov, E.Z. Kurmaev, R.J. Green, I.S. Zhidkov, S.S. Kim, L. Cui, N.V. Gavrilov, S.O. Cholakh, A. Moewes, J. Phys. Chem. C 118 (2014) 28143–28151.

[48] M.V. Sofianou, M. Tassi, V. Psycharis, N. Boukos, S. Thanos, T. Vaimakis, Jiaguo Yu, C. Trapalis, Catal. B: Environ. 162 (2015) 27–33.

[49] P. Zhang, J. Liu, Z. Zhang, Chem. Lett. 33 (2004) 1242–1243.

[50] J. Jeong, K. Sekiguchi, K. Sakamoto, Chemosphere 57 (2004) 663–671.

[51] F. Parrino, G. Cameraroda, V. Loddo, G. Palmisano, V. Augugliaro, Water Res. 50 (2014) 189.

[52] J. Jia, P. Zhang, L. Chen, Appl. Catal. B: Environ. 189 (2016) 210–218.

[53] J. Wang, J. Li, C. Jiang, P. Zhou, P. Zhang, J. Yu, Appl. Catal. B: Environ. 204 (2017) 147–155.

[54] H. Huang, H. Lu, Y. Zhan, G. Liu, Q. Feng, H. Huang, M. Wu, X. Ye, Appl. Surf. Sci. 391 (2017) 662–667.

[55] R. Malik, V.K. Tomer, V. Chaudhary, M.S. Dahiya, P.S. Rana, S.P. Nehra, S. Duhan, Chemistryselect 1 (2016) 3247–3258.

[56] P. Zhang, F. Liang, Y. Gang, Q. Chen, W. Zhu, J. Photochem. Photobiol. A Chem. 156 (2003) 189–194.

[57] F. He, J. Li, T. Li, G. Li, Chem. Eng. J. 237 (2014) 312–321.

[58] J. Zhong, J. Wang, L. Tao, M. Gong, L. Zhimin, Y. Chen, J. Hazard. Mater. 139 (2007) 323–331.